A line scanned light-sheet microscope with phase shaped self-reconstructing beams

Florian O. Fahrbach[1,2] **and Alexander Rohrbach**[1,2]

[1]*Laboratory for Bio- and Nano-Photonics, Department of Microsystems Engineering - IMTEK,*
University of Freiburg, Germany
[2]*Centre for Biological Signalling Studies (bioss), University of Freiburg, Germany*
[3]*fahrbach@imtek.de*
[4]*rohrbach@imtek.de*

Abstract: We recently demonstrated that Microscopy with Self-Reconstructing Beams (MISERB) increases both image quality and penetration depth of illumination beams in strongly scattering media. Based on the concept of line scanned light-sheet microscopy, we present an add-on module to a standard inverted microscope using a scanned beam that is shaped in phase and amplitude by a spatial light modulator. We explain technical details of the setup as well as of the holograms for the creation, positioning and scaling of static light-sheets, Gaussian beams and Bessel beams. The comparison of images from identical sample areas illuminated by different beams allows a precise assessment of the interconnection between beam shape and image quality. The superior propagation ability of Bessel beams through inhomogeneous media is demonstrated by measurements on various scattering media.

OCIS codes: (230.6120); (170.2520) Fluorescence microscopy, (180.6900) 3D microscopy; (260.2710) Light propagation in inhomogeneous optical media

---

References and links

1. F. Pampaloni, E. G. Reynaud, and E. H. K. Stelzer, "The third dimension bridges the gap between cell culture and live tissue," Nat. Rev. Mol. Cell Biol. **8**(10), 839–845 (2007).
2. V. Ntziachristos, "Going deeper than microscopy: the optical imaging frontier in biology," Nat. Methods **7**(8), 603–614 (2010).
3. A. H. Voie, D. H. Burns, and F. A. Spelman, "Orthogonal-plane fluorescence optical sectioning: three-dimensional imaging of macroscopic biological specimens," J. Microsc. **170**(Pt 3), 229–236 (1993).
4. J. Huisken, J. Swoger, F. Del Bene, J. Wittbrodt, and E. H. K. Stelzer, "Optical sectioning deep inside live embryos by selective plane illumination microscopy," Science **305**(5686), 1007–1009 (2004).
5. H. U. Dodt, U. Leischner, A. Schierloh, N. Jährling, C. P. Mauch, K. Deininger, J. M. Deussing, M. Eder, W. Zieglgänsberger, and K. Becker, "Ultramicroscopy: three-dimensional visualization of neuronal networks in the whole mouse brain," Nat. Methods **4**(4), 331–336 (2007).
6. P. J. Keller, A. D. Schmidt, J. Wittbrodt, and E. H. Stelzer, "Reconstruction of zebrafish early embryonic development by scanned light sheet microscopy," Science **322**(5904), 1065–1069 (2008).
7. J. A. N. Buytaert, and J. J. J. Dirckx, "Design and quantitative resolution measurements of an optical virtual sectioning three-dimensional imaging technique for biomedical specimens, featuring two-micrometer slicing resolution," J. Biomed. Opt. **12**(1), 014039 (2007).
8. J. Huisken, and D. Y. Stainier, "Selective plane illumination microscopy techniques in developmental biology," Development **136**(12), 1963–1975 (2009).
9. E. G. Reynaud, U. Krzic, K. Greger, and E. H. K. Stelzer, "Light sheet-based fluorescence microscopy: more dimensions, more photons, and less photodamage," HFSP J **2**(5), 266–275 (2008).
10. W. T. Welford, "Use of Annular Apertures to Increase Focal Depth," J. Opt. Soc. Am. **50**(8), 749–753 (1960).
11. J. W. Y. Lit, and R. Tremblay, "Focal Depth of a Transmitting Axicon," J. Opt. Soc. Am. **63**(4), 445–449 (1973).
12. J. Durnin, J. J. Miceli, Jr., and J. H. Eberly, "Diffraction-free beams," Phys. Rev. Lett. **58**(15), 1499–1501 (1987).
13. Z. Bouchal, J. Wagner, and M. Chlup, "Self-reconstruction of a distorted nondiffracting beam," Opt. Commun. **151**(4-6), 207–211 (1998).
14. V. Garcés-Chávez, D. McGloin, H. Melville, W. Sibbett, and K. Dholakia, "Simultaneous micromanipulation in multiple planes using a self-reconstructing light beam," Nature **419**(6903), 145–147 (2002).
15. F. O. Fahrbach, P. Simon, and A. Rohrbach, "Microscopy with self-reconstructing beams," Nat. Photonics (2010), doi: 10.1038/nphoton.2010.204.
16. J. Huisken, and D. Y. R. Stainier, "Even fluorescence excitation by multidirectional selective plane illumination microscopy (mSPIM)," Opt. Lett. **32**(17), 2608–2610 (2007).

#134155 - $15.00 USD Received 7 Sep 2010; accepted 13 Oct 2010; published 4 Nov 2010

17. A. Rohrbach, "Artifacts resulting from imaging in scattering media: a theoretical prediction," Opt. Lett. **34**(19), 3041–3043 (2009).
18. R. D. L. Hanes, M. C. Jenkins, and S. U. Egelhaaf, "Combined holographic-mechanical optical tweezers: construction, optimization, and calibration," Rev. Sci. Instrum. **80**(8), 083703 (2009).
19. C. W. McCutchen, "Generalized Aperture and the Three-Dimensional Diffraction Image," J. Opt. Soc. Am. **54**(2), 240–244 (1964).
20. Y. Roichman, and D. G. Grier, "Projecting extended optical traps with shape-phase holography," Opt. Lett. **31**(11), 1675–1677 (2006).
21. A. Jesacher, C. Maurer, A. Schwaighofer, S. Bernet, and M. Ritsch-Marte, "Near-perfect hologram reconstruction with a spatial light modulator," Opt. Express **16**(4), 2597–2603 (2008).
22. M. Agour, E. Kolenovic, C. Falldorf, and C. von Kopylow, "Suppression of higher diffraction orders and intensity improvement of optically reconstructed holograms from a spatial light modulator," J. Opt. A **11**, 105405 (2009).
23. E. G. van Putten, I. M. Vellekoop, and A. P. Mosk, "Spatial amplitude and phase modulation using commercial twisted nematic LCDs," Appl. Opt. **47**(12), 2076–2081 (2008).

1. Introduction

High-resolution three-dimensional images of extended samples are of increasing importance due to a paradigm shift in biological and medical research away from cover-slip based two-dimensional experiments [1]. However, most established microscopic techniques expose significant loss in contrast and resolution when imaging deep in thick media [2]. A fluorescence microscopy technique generally called "light sheet-based fluorescence microscopy" (LSFM) [3–7] is well adapted to the needs of life-science imaging [8,9]. The advantages of LSFM include high acquisition speed and low exposure of the sample to illumination light.

In LSFM, the sample is illuminated by a light sheet a thin slice at a time. Fluorescence is detected orthogonally to the light sheet by a detection objective lens and imaged onto a camera sensor. The light sheet can either be formed coherently by the use of cylindrical optics [3–5,7] or incoherently by lateral scanning of a (circularly symmetric) Gaussian beam focused into the sample using a microscope objective lens [6].

Microscopy with self-reconstructing beams (MISERB) is based on the use of laterally scanned Bessel beams for sample illumination. Bessel beams can be created using annular apertures [10] or axicons [11] and show an increased depth of focus, i.e. the transverse intensity profile of Bessel beams changes only very little over a considerable distance. This propagation invariance was explained by strongly reduced diffraction in free-space [12]. Moreover, Bessel beams are able to self-reconstruct, i.e. regain their initial profile behind isolated obstacles [13,14]. Only recently it has been shown that Bessel-beams are able to self-reconstruct even inside inhomogeneous, scattering media [15]. By exploiting these properties, MISERB addresses the following three factors limiting the image quality in LSFM. First, due to light's natural beam spreading, there is a tradeoff between the illumination beam's depth of field and its beam waist. An improvement of the axial resolution, i.e in optical sectioning, can only be achieved by a stronger axial focusing of the light sheet, thereby reducing the depth of field of the illumination beam [7]. Second, as the illumination light path lies in the plane to be imaged, scattering and absorption result in strongly visible artifacts in the image such as dark and bright stripes behind scatterers (ghost images). These artifacts can, so far, only be suppressed in visibility by tilting the light sheet in the image plane [16]. Third, scattering causes additional non-uniform spreading of the illumination beam along the propagation into the sample. This leads to a limited penetration depth, i.e. a decrease in image quality and signal strength along the illumination axis.

Altogether, the robustness of Bessel-beams against scattering enables MISERB increased image quality in inhomogeneous media because of weaker ghost images [17]. An increase in penetration depth in dense media like human skin was also measured [15], which allows the observation of details at a depth within samples that has not been accessible so far.

In this paper, we show how MISERB can be technically realized by using an add-on to a standard inverted microscope with a spatial light modulator (SLM) to shape the illumination beam. Analytical formulas allow comparing radial intensity profiles and energy contents of Bessel and Gaussian beams in dependence of the depth of field. Furthermore, we discuss

#134155 - $15.00 USD Received 7 Sep 2010; accepted 13 Oct 2010; published 4 Nov 2010

computer holograms for shaping three different illumination beams: a static light sheet, a Gaussian and a Bessel beam. Special emphasis is put on the reduction of SLM-induced artifacts that deteriorate image quality by creating additional background or uneven sample illumination. Finally, we compare images from extended inhomogeneous objects applying different illumination beams. The results confirm that image quality and penetration depth for illumination of artificial and biological samples can be improved by the use of self-reconstructing Bessel beams.

2. The setup

A microscope for the illumination of samples with light beams shaped by a spatial light modulator (SLM) perpendicular to the detection optical axis has been developed. The device used for sample positioning is discussed in section 2.2. The optical part of the setup consists of a standard inverted microscope (Axiovert 200M, Zeiss) with suitable detection objective lenses (DO) (Achroplan 63x/0.95 W, 40x/0.8 W or 20x/0.5 W, Zeiss) and an add-on module for sample illumination. Hence it is possible to use the features provided by a standard microscope. The add-on module as sketched in Fig. 1 consists of three parts: the laser unit, the beam shaping optics the illumination optics.

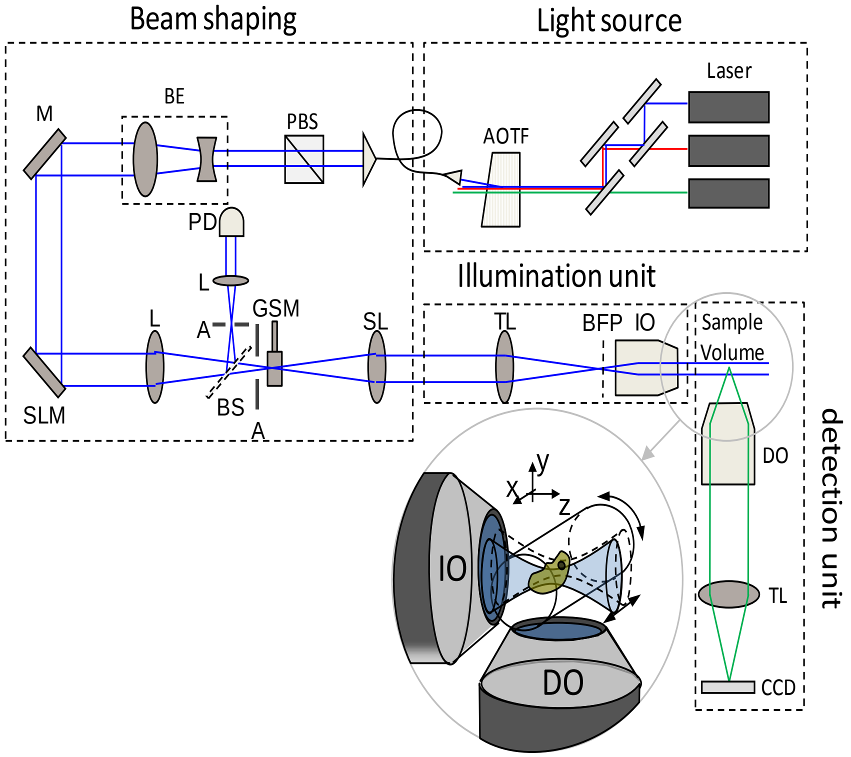

Fig. 1. Schematic drawing of the setup. For explanation and acronyms see body text of section 2.

As a light source a multi-laser unit (Laser module LSM 510 - Release 3.2, Zeiss) with an acousto-optic tunable filter (AOTF) for laser selection and fast intensity modulation is used. A single mode fiber transfers the light to the beam-shaping unit situated on an optical table along with the microscope. For a better definition of the polarization, a polarizing beam splitter (PBS) regulates polarization modulation induced by mechanical vibrations of the fiber. The PBS transforms polarization modulation into intensity modulation that can be compensated for by a feedback loop which will be described later. The beam is expanded by a modular beam expander (BE) (bm.x VIS-YAG, Linos Photonics) to homogenously illuminate the SLM (LC-

Received 7 Sep 2010; accepted 13 Oct 2010; published 4 Nov 2010

R2500, Holoeye). The hologram is imaged into the sample volume by four lenses. The first lens (L) images the SLM's far-field diffraction pattern onto a galvanometric scan mirror (GSM) (M2, GSI). The illumination beam is scanned laterally in the focal plane of the detection objective lens (DO) to illuminate the full field of view. Therefore, the tilt angle of the galvanometric scan mirror (GSM) is translated into a lateral displacement of the illumination beam in the sample volume by a telecentric lens system and the illumination objective lens (IO) (LD Achroplan 20x/0.40 Corr, Zeiss). The telecentric lens system consists of a scan lens (SL) and the IO's tube lens (TL), a Laser-monochromat (Linos) and an Achromat (Linos). Both have a focal length of f = 120mm. The tube lens (TL) and the illumination objective lens (IO) are integrated in a kinematic mount which is placed on the stage of the microscope. It is thus easily removable to facilitate access and can be repositioned with high accuracy.

2.1 Laser intensity stabilization

Intensity fluctuations of the illumination light are detrimental since the scanning of the beam in the image plane translates any temporal modulation into a spatial modulation. Stripes become visible at high scanning frequencies, where the beam displacement during an intensity fluctuation period is larger than the lateral beam size. The modulation of the diffraction efficiency of the SLM results in an intensity modulation that has a complex shape with a hologram-dependent amplitude of up to 30% at a frequency of 70Hz and a much higher cut-off frequency. This is corrected for by an electronic feedback circuit, thereby also eliminating other possible intensity fluctuations. A pellicle beam splitter BS (BP108, Thorlabs) placed in front of the scanning mirror (GSM) reflects a small part (~8%) of the SLM's diffraction pattern that is imaged onto a reference photodiode (PDR-S, TEM) with a lens. The signal is used as input for laser intensity stabilization using a feedback loop (NoiseEater 2.1, TEM, Germany) to steer the AOTF transmission. The amplitude modulation by the SLM can also be reduced by adapting the polarization of the incoming light [18]. This method was not chosen due to the observed loss in diffraction efficiency.

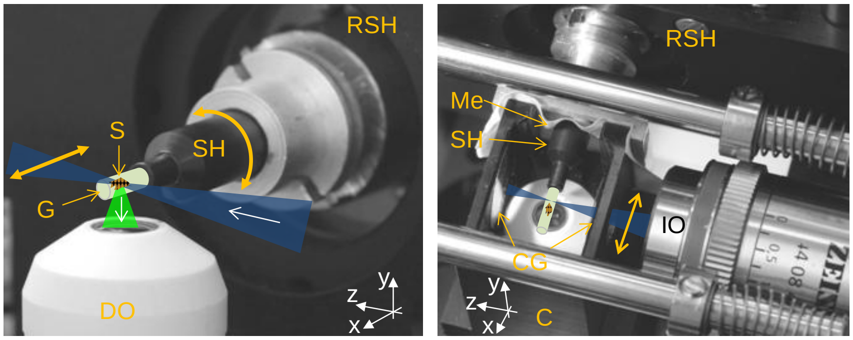

Fig. 2. Photographs of the sample holder and positioner. The sample (S) is fixed in an agarose gel cylinder (G) held by a sample holder (SH) that can be rotated by a rotating sample holder (RSH). It is introduced through a hole in a flexible membrane (Me) into the sample chamber (C) that holds the sample in the immersion liquid. Beams focused by the illumination objective (IO) and scanned in the focal plane of the detection objective lens (DO) excite fluorophores only in a thin layer within the sample.

2.2 Sample mounting and manipulation

Samples are mounted in Agarose gel cylinders [4,9]. In contrast to stand-alone light-sheet microscopes the use of a standard microscope imposes the restriction that the detection optical axis is vertical. Therefore, the gel cylinder has to be mounted horizontally (see Fig. 2). For acceptable stability, gel cylinders with diameters >1.2mm and Agarose concentrations >1% are used. The capillary containing the Agarose gel cylinder is introduced into a holder and the gel is pushed out of the capillary. The mount, tightly gripping the Agarose, serves as an interface to the positioning and rotating device (RSH). As measurements are performed in an immersion medium, e.g water, a chamber holding the liquid has to be used [see Fig. 2(b)]. The chamber is made from biocompatible, black Delrin and features sealed openings for both the water dipping detection objective lens and the sample holder. A long working-distance air immersion objective lens is used for illumination through a hole in the chamber that is sealed by a coverglass. Spherical aberrations of the illumination beam are introduced by the refractive index mismatch. These depend on the distance that the light propagates through the water-filled chamber. The chamber is thus designed in a way that this distance is reduced to a minimum, which is determined by mechanical restrictions such as objective lens dimensions and space needed for sample positioning. As samples are introduced sideways, the opening has to be sealed in a way flexible enough still to allow positioning of the sample. Acting as a flexible membrane a piece of latex glove with a small cut (Me) through which samples are introduced is sufficient.

The capillary mount is fixed in a combined positioner-rotator-unit. The unit is mounted on the microscope stage allowing the manual lateral (horizontal) displacement of the sample in the xz-plane. A three-dimensional image stack is recorded by moving the sample along the detection optical y-axis in discrete steps through the focal plane of the DO using a piezo positioner (NanoSX400, PiezoJena). Rough adjustment is possible by a manual translation stage. A rotary support (custom modification based on DMT40, OWIS) allows the orientation of the gel cylinder along its symmetry axis. This can be useful when imaging non-symmetric objects, e.g. a piece of human skin.

3. Focal depths and diameters of illumination beams

The amount and distribution of the energy carried in beams with identical depths of focus are important properties of illumination beams, especially for microscopy purposes as in our MISERB system [15]. In order to understand their intensity distribution, analytical formulas for the radial intensity profile for conventional (Gaussian) and Bessel beams will be derived in the following.

Ideal zero-order Bessel beams have a radial intensity profile given by $I(r) = I_0\cdot|J_0(k_\mathrm{r}\, r)|^2$, J_0 being the Bessel function of the 0th order. $I(r)$ does not depend on the propagation distance z. The angular spectrum is infinitely thin and can be written as $\tilde{E}(k_r) = \delta\left(k_r - k_0 NA\right)$, where k_0 is the wave-vector in vacuum and k_r its radial component and $NA = n\cdot\sin\alpha$ the numerical aperture of the focusing lens. The strongly reduced beam spreading can be attributed to the suppression of diffraction in free space, which is why Bessel beams are also called non-diffracting beams [12].

However, the realistic case of a (zero-order) Bessel beam that has an angular spectrum with a finite ring width can be described by

$$\tilde{E}(k_r) = \tilde{E}_0\left(\Theta(k_0 NA - k_r) - \Theta(\sqrt{\varepsilon}\, k_0 NA - k_r)\right), \tag{1}$$

where $\Theta(x)$ denotes the Heaviside step function. $\varepsilon<1$ is the ring width parameter, i.e the area ratio of the inner to the outer disc. For $\varepsilon = 0$, the back aperture is homogeneously illuminated and a conventional beam with a limited depth of field $\Delta z \propto \lambda/(1-\cos\alpha)$ is created. The intensity profile $I(r) = |\mathrm{HTf}|^2$ is obtained from Eq. (1) by a Hankel-Transformation (HT). Normalization of the beam intensity to one results in

$$I_{Bessel}(r) = \left[\frac{2}{(2\pi)^2}\frac{1}{k_0 NA(\varepsilon-1)}\frac{1}{r}\left(J_1\left(k_0 NA\, r\right) - \sqrt{\varepsilon} J_1\left(\sqrt{\varepsilon}\, k_0 NA\, r\right)\right)\right]^2. \tag{2}$$

The total energy transported per time up to radius R is given by

$$W(r) = 2\pi\int_0^R I(r) r dr. \tag{3}$$

#134155 - $15.00 USD
Received 7 Sep 2010; accepted 13 Oct 2010; published 4 Nov 2010

The depth of field (DOF) of beams with an angular spectrum described by Eq. (1) can be estimated using the width of the spectrum's projection on the k_z –axis [19], defined by $k_z = \left(k_0^2 - k_r^2\right)^{1/2}$ via the Ewald sphere:

$$\Delta k_z = k_0\left(\sqrt{n^2 - \varepsilon NA^2} - \sqrt{n^2 - NA^2}\right). \tag{4}$$

which is related to the DOF by

$$\Delta z = q / \Delta k_z, \tag{5}$$

where the parameter q depends on the exact shape of $\tilde{E}(k_z)$ and the acceptable intensity drop-off. For a rectangular shape of $\tilde{E}(k_z)$, the intensity-FWHM Δz is obtained with $q = 5.56$.

The radial intensity distributions of one conventional and two Bessel beams with equal DOFs are compared in Fig. 3. Bessel beams with a DOF of Δz = 100µm are obtained by NA = 0.24 and ε = 0.8 or by NA = 0.34 with ε = 0.9. This corresponds to a homogeneous circular illumination (ε = 0) of the BFP focused with NA = 0.11. Plots of the radial intensity $I(r)$ according to Eq. (2) can be seen in Fig. 3(a). A large fraction of the Bessel beam's energy distribution is located in the ring system so that the beam covers a large transverse area. For equivalent energies in the area of the Airy disc of the standard beam, the Bessel beam carries – approximately 3 (NA = 0.24, ε = 0.8) to 5 (NA = 0.34, ε = 0.9) times more total energy, as can be seen in Fig. 3(b). The Bessel beam's ring system is essential for the long DOF, but for imaging applications perpendicular to the Bessel beam axis, it may lead to inferior optical sectioning and decreased contrast, as will be discussed later. However, for equivalent DOFs, Bessel beams are produced at higher NAs as conventional beams resulting in a narrower central lobe [see inset in Fig. 3(a)]. An important difference between conventional and Bessel beams lies in the fact that in contrast to conventional beams where the beam diameter increases by a factor of $\sqrt{2}$ over the focal range, for Bessel beams the size of the thin central lobe is maintained over the whole depth of field.

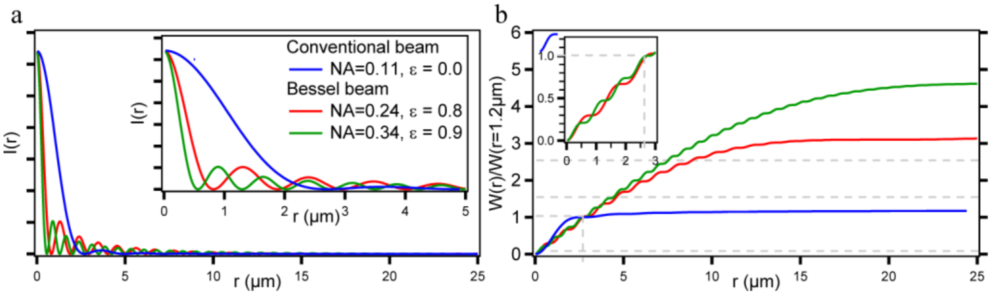

Fig. 3. Radial Intensity of three beams with equal depth of focus Δz = 100µm. A Gaussian beam (NA = 0.11) shown in blue, and two Bessel beams (NA = 0.24, ε = 0.8 and NA = 0.34 & ε = 0.9) shown in red and green, respectively. A normalization of W(r) was applied so that all beams carry the same amount of energy up to the radius of a conventional beam. In this case r(NA = 0.11) = 2.7µm.

4. Holographic generation of illumination beams

A beam with field $E_{\text{in}}(x,y)$ can be shaped by a hologram $h(x,y)$ generated with an SLM to obtain a field

$$E(x,y) = E_{in}(x,y)\cdot h(x,y). \tag{6}$$

The hologram has the general form

$$h(x,y) = t(x,y)\cdot e^{i\delta\phi(x,y)}, \tag{7}$$

where $t(x,y)$ denotes the amplitude modulation and $\delta\phi(x,y)$ the phase modulation. For phase-only SLMs no gradual amplitude modulation is possible meaning that $t(x,y)$ is either 0 or 1. A small amplitude modulation in the dependence of the phase modulation $t(\phi(x,y))$ that occurs in practice is neglected at this point. The ideal intensity distribution in the far-field or the focus of a lens is then obtained by a Fourier transform

$$I_{ideal}(k_x,k_y) = \left| FT\left\{ h(x,y)\cdot E_{in}(x,y) \right\} \right|^2 . \tag{8}$$

4.1 Spatial separation of the SLM's diffraction pattern

The SLM has a pixellated display with a fill-factor of 93%, meaning that there are gaps between the active pixels. The SLM therefore acts as a two-dimensional rectangular grating of which the field reflection coefficient is described by $t_{pix}(x,y)$. A field incident on the SLM is additionally modulated by the periodic function $t_{pix}(x,y)$, such that the diffracted intensity is given by

$$\begin{aligned} I_{total}(k_x,k_y) &= \left| FT\left\{ t_{pix}(x,y)\cdot h(x,y)\cdot E_{in}(x,y) \right\} \right|^2 \\ &= \left| FT\left\{ t_{pix}(x,y) \right\} * FT\left\{ h(x,y)\cdot E_{in}(x,y) \right\} \right|^2 \end{aligned} \tag{9}$$

where * indicates a convolution. The periodic distribution FT$\{t_{pix}(x,y)\}$ will multiply the far-field diffraction pattern $I_{\mathrm{ideal}}(k_x,k_y)$ that is generated by the ideal phase hologram $h(x,y)$. I_{total} features sidebands or higher diffraction orders and a prominent zero-frequency contribution. These have to be eliminated because they create additional background in light-sheet microscopy.

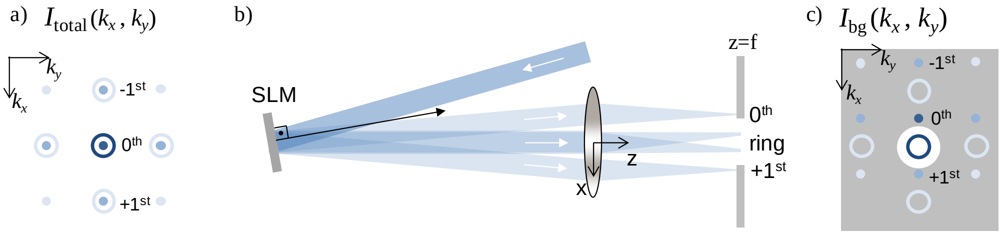

Fig. 4. Scheme for the separation of hologram diffraction pattern from background created by the pixellation of the SLM's display. The figure shows an example for an axicon hologram. A blazed grating $\phi_{\mathrm{bg}}(x,y) = x\cdot a$ is added to shift the hologram's far-field diffraction image between 0th and 1st order caused by the SLM's pixellation. A cross-section of the far-field diffraction intensity for an axicon without and with an additional blazed grating is shown in part (a) and (c), respectively. A sketch of the optical path is shown in (b). All unwanted intensity like higher orders can be removed by a circular stop shown in gray in (c).

Figure 4(a) shows an example of $I_{\mathrm{total}}(k_x,k_y)$ for a hologram creating a ring-shaped intensity distribution in the far field. Higher diffraction orders $n \neq +1$ created by the SLM's reflectivity can be easily eliminated by a circular stop centered around the 0th diffraction order. But the central spot [see Fig. 4(a)] is difficult to block, especially for symmetric phase holograms that result in a distribution of $I_{\mathrm{ideal}}(x,y)$ around the spot. An effective method to circumvent this is to introduce an asymmetry into the hologram. A blazed grating $\phi_{\mathrm{bg}}(x,y) = x\cdot a$ is added to the hologram yielding the intensity distribution

$$I_{bg}(k_x,k_y) = \left| FT\left\{ t_{pix}(x,y) \right\} * FT\left\{ h(x,y)\cdot e^{i\phi_{bg}(x,y)}\cdot E_{in}(x,y) \right\} \right|^2 . \tag{10}$$

The optimal slope $a = 2\pi/p_{\mathrm{bg}}$ shifts $I_{\mathrm{ideal}}(k_x, k_y)$ to the center between the 0th and the + 1st (lateral) order, so that there is no overlap with the central spot of the 0th diffraction order. If the SLM is positioned under an angle such that $I_{\mathrm{ideal}}(k_x, k_y)$ lies centrally on the optical axis [see Fig. 4(b)] a circular stop [see white area of transmission in Fig. 4(c)] can be used to block all higher orders as well as the central spot of the 0th order.

4.2 Holograms for beam shaping and positioning

The exact adjustment of the illumination beam in light-sheet based microscopy is crucial to the image quality. Therefore, in this section, details on the shaping and positioning of illumination beams with an SLM are presented. As can be seen in fig. 1, the SLM is imaged by 4 lenses in an 8f-configuration into the sample volume. In this section, the 4f-system consisting of the scan lens (SL) and the tube lens (TL) is omitted as it only contributes a magnification $M = f_{TL}/f_{SL}$.

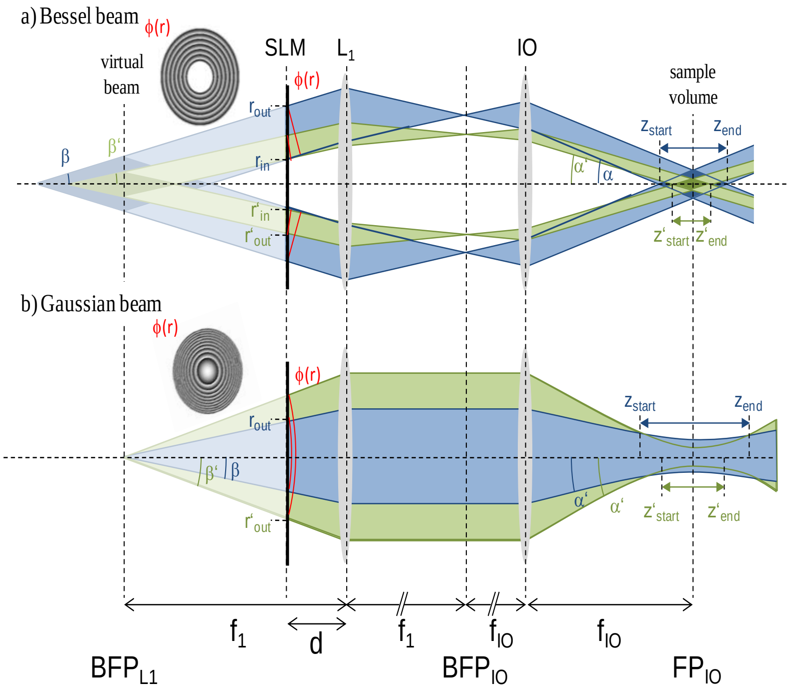

Fig. 5. The optical path for holographic beam shaping and positioning. The figure shows the generation of Bessel (a) and Gaussian beams (b) by applying adequate spatial phase distributions $\phi(r)$ (shown in red and as insets) on the beam using the SLM. A telecentric 4f lens system images a virtual beam created by the SLM (placed in a distance $d<f_1$ to the lens L1) into the sample volume. A conical phase with ring-shaped aperture (shown in red) is used for Bessel beams (a). For Gaussian beams, a spherical phase with a circular aperture is applied (b). Beams with short and long depth of field z_{end}-z_{start} are shown in green and blue, respectively.

The SLM is positioned at a distance *d* to the lens L_1 that is smaller than its focal length f_1 (see Fig. 5). A hologram is applied so that the virtual image of a beam is imaged into the sample volume by the 4f-system consisting of L_1 and IO. Thereby, the optical path is shortened. Additionally, the afocal position of the SLM offers an elegant possibility to use the SLM for the generation of Bessel beams and conventional beams at the same axial position within the sample volume.

Each hologram consists of three parts, as depicted in Fig. 6. After adding a phase grating (see previous section) to the hologram phase $\delta\phi(x,y)$, we multiply an aperture function $t(x,y)$ to steer the position and size of the beam. Details on the aperture will be given in the next section. In the following, holograms for the generation of Bessel beams, conventional beams and light-sheets as shown in Fig. 7 will be presented.

Received 7 Sep 2010; accepted 13 Oct 2010; published 4 Nov 2010

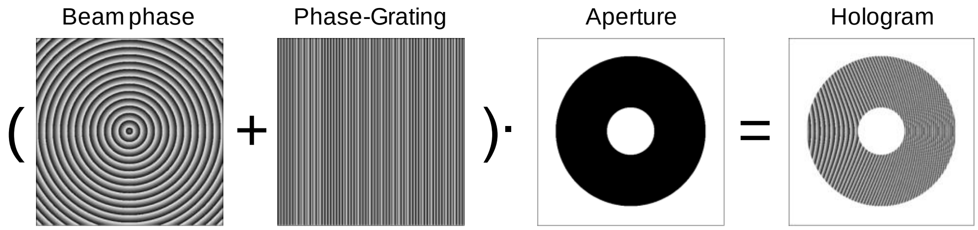

Fig. 6. Composition of holograms. Schematic example shows a phase axicon and a ring aperture.

According to Eq. (7) the hologram for the generation of a Bessel beam is given by

$$\delta\phi(x,y) = -k_r \cdot r \tag{11}$$

$$t(x,y) = \Theta\left(r - r_{out}\right)\cdot\Theta\left(r_{in} - r\right) \tag{12}$$

where $r = \sqrt{x^2 + y^2}$ is the radial distance from the optical axis (and the SLM center) and $k_r = 2\pi/p$ is the slope of the phase axicon. The amplitude modulation is given by an annular aperture with inner and outer radius defined by r_{in} and r_{out}, respectively [see Fig. 5(a)]. The phase of the Bessel beam is a cone making light propagate at an angle $\beta = arctan(\lambda/p) = asin(k_r/k_0)$ to the optical axis [see Fig. 5(a)]. In the object plane, the Bessel beam is formed by the interference of plane waves with their wave-vector lying on the surface of a cone with angle $\alpha = \beta/M,$ where $M = f_{IO}/f_{L1}{\cdot}f_{TL}/f_{SL}$ is the magnification of the telecentric lens system. The illumination beam's NA is determined by $NA = n{\cdot}sin\alpha = n{\cdot}sin(k_r/k{\cdot}M^{-1})$. The dimensions of the diamond-shaped area of interference where the Bessel beam is formed, i.e. the central lobe with the surrounding ring system, can be estimated by geometrical considerations [see Fig. 5(a)], yielding length dz and radius dr:

$$dz = -M^2 \cdot \frac{r_{\mathrm{out}} - r_{\mathrm{in}}}{tan\beta} \tag{13}$$

$$dr = M \cdot \left(r_{\mathrm{out}} - r_{\mathrm{in}}\right). \tag{14}$$

An example is shown in Fig. 7(a). The radii of the annular aperture can thus be used to manipulate the position and the depth of focus, i.e. the self-reconstruction distance of the Bessel beam. The exact lateral and axial beam profile (the beam's depth of field Δz) is dependent on the beam's intensity profile at the SLM $E_{in}(x,y)$ and the amplitude hologram $t(x,y)$ applied to the SLM. Using Eqs. (13) and (14) it is evident that for a given beam length dz the radius $dr = -M{\cdot}\Delta z/\tan\beta$ increases for a steeper slope $k_r = k_0{\cdot}\mathrm{asin}(\beta)$ of the phase hologram, which corresponds to a higher focusing NA. This means, that a Bessel beam created by a higher NA carries more energy in the ring system for an equivalent depth of field, as shown in fig. b. For Bessel beams, there are two parameters to tune the depth of field: the radii r_{in} and r_{out} of the aperture and slope of the phase k_r.

For comparison, a conventional beam can be generated by the quadratic approximation to a spherical hologram phase given by

$$\delta\phi(x,y) = -k_0 \cdot r^2 / 2\rho \tag{15}$$

$$t(x,y) = \Theta\left(r - r_{max}\right) \tag{16}$$

where k is the wavenumber and ρ is the radius of the spherical wavefront. Ideally we find $\rho = f_1 - d$ as shown in Fig. 5(b). The radius of the hologram's aperture r_{max} determines the NA of the illumination beam to which it is linearly proportional. An example is shown in Fig. 7(b). In contrast to the Bessel-beams, there is a fixed ratio between the beam's width and depth of field

Received 7 Sep 2010; accepted 13 Oct 2010; published 4 Nov 2010

which is fully determined by the NA. Axial positioning is possible by changing the lens phase radius ρ. This gives rise to spherical aberrations, which are negligible for the small NAs commonly used for sample illumination.

The creation of a light sheet is possible using a cylindrical lens with a slit aperture according to

$$\delta\phi(x,y) = -k \cdot x^2 / 2\rho \tag{17}$$

$$t(x,y) = \Theta\left(|x| - w_x/2\right) \cdot \Theta\left(|y| - w_y/2\right). \tag{18}$$

In analogy to spherical holograms it is possible to adapt the DOF by changing the aperture width of the cylindrical lens w_x. Positioning along the optical axis is possible via ρ. The width of the light sheet can be tuned by the width of the lens w_y. An example hologram is shown in Fig. 7(c).

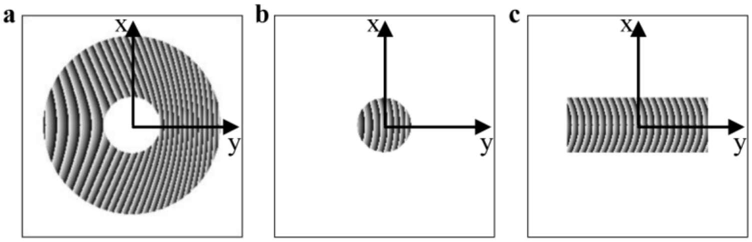

Fig. 7. Phase of holograms for generating illumination beams. The hologram for Bessel (a) and Gaussian beam (b) and a static light-sheet (c) is shown in grayscale where a phase-shift of $\delta\phi = 0$ is indicated in white and $\delta\phi = 2\pi$ in black.

4.3 Low-pass-filtering of the amplitude mask against axial intensity oscillations

The hard clipping apertures *t(x,y)* on the SLM (see e.g. Figure 6) result in lateral intensity undulations $\tilde{I}(k_x,k_y) = |\tilde{E}(k_x,k_y)|^2$ in the BFP (see Fig. 5), i.e. in pronounced sidelobes of the illumination beam, which are detrimental to the image quality. But more importantly, they cause undulations in the axial beam intensity. In this section low-pass filtered smooth apertures and a special implementation using an SLM are introduced.

The lateral field in the BFP, the spectrum $\tilde{E}(k_x,k_y)$ is a convolution of the spectra of the phase hologram and the amplitude aperture function, respectively and can be written as

$$\tilde{E}\left(k_x,k_y\right) = FT\left(e^{i\phi(x,y)} \cdot t(x,y)\right) = FT\left(e^{i\phi(x,y)}\right) * \tilde{t}\left(k_x,k_y\right). \tag{19}$$

If $\tilde{t}\left(k_x,k_y\right)$ is periodic the convolution results in periodic side-lobes in the angular spectrum that translate into a periodic axial modulation of the beam due to the Talbot-Effect. For example, if the amplitude function *t(x,y)* is a circular aperture, then the spectrum $\tilde{E}$ is the Fourier-Transform of the phase-only hologram $FT\left(e^{i\phi(x,y)}\right)$ convolved, i.e. smoothed, with an Airy pattern $\tilde{t}\left(k_x,k_y\right)$. In the case of an axicon phase-hologram, the convolution of the Airy pattern with the ring-shaped spectrum creates auxiliary concentric rings. As each ring (k_r-component) produces a Bessel beam with a different k_z-component of the wave-vector, these run out of phase along the propagation axis and produce a (periodic) intensity variation. This is undesirable for illumination purposes and it can be reduced by applying a smoother aperture on the SLM, i.e. by applying a Gaussian low-pass-filter $\exp\left(-\left(r/r_{LP}\right)^2\right)$ to the aperture function according to the aperture function

$$t_{LP}(x,y) = t(x,y) * e^{-\left(r/r_{LP}\right)^2} \tag{20}$$

Received 7 Sep 2010; accepted 13 Oct 2010; published 4 Nov 2010

so that the spectrum is equal to

$$\tilde{E}\left(k_x,k_y\right) = FT\left(e^{i\phi(x,y)}\right) * \left(\tilde{t}\left(k_x,k_y\right)\cdot e^{-\left(k_r\cdot r_{LP}/2\right)^2}\right) \tag{21}$$

For example, in the case of a circular aperture $t(r)=\theta\left(r-r_{\max}\right)$ the spectrum is given by

$$\tilde{E}(k_r) = FT\left(e^{i\phi(x,y)}\cdot\left(\theta\left(r-r_{\max}\right) * e^{-\left(r/r_{LP}\right)^2}\right)\right) \propto FT\left(e^{i\phi(x,y)}\right) * \left(\frac{J_1\left(k_r r_{\max}\right)}{k_r r_{\max}}\cdot e^{-\left(k_r\cdot r_{LP}/2\right)^2}\right). \tag{22}$$

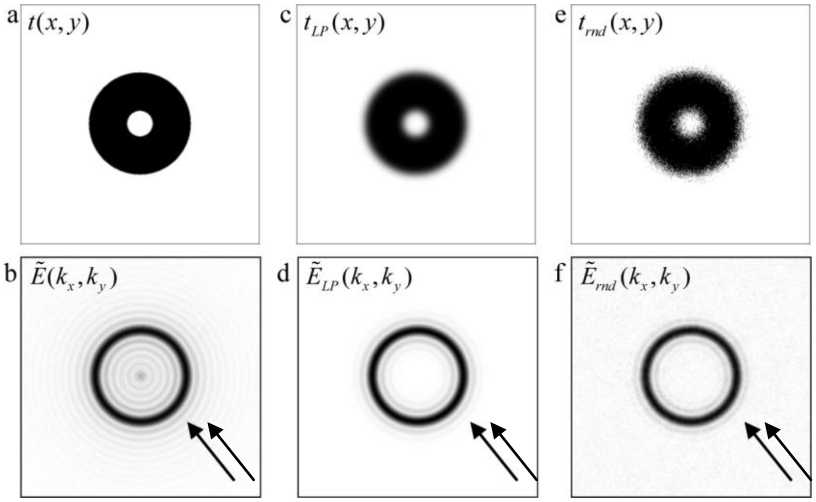

Fig. 8. Aperture low-pass filtering against axial intensity oscillations. Numerical simulations illustrate that additional rings (b) visible in the spectrum of the ring aperture (a) can be suppressed by low-pass filtering of the aperture (c). The result is shown in (d). The effect of a random pixel mask (e) is shown in (f).

The rings of the Airy disc $J_1(k_r r_{\max})/k_r r_{\max}$ resulting from the sharp aperture are suppressed strongly enough by the Gaussian function to avoid on-axis intensity oscillations of the beam for $r_{LP} < r_{\max}\cdot 3.83/5$ (as the first root of the Bessel-Function $J_1(k_r r_{max})$ lies at $k_r r_{max} = 3.83$) as can be seen in Figs. 8(a)–8(d). For small r_{LP} the low-pass filter is equivalent to a Gaussian illumination of the hologram. By applying a low-pass filter with a very low r_{LP} it is possible to generate Gaussian beams using the hologram described in Eqs. (15) and (16).

The application of low-pass-filtered apertures requires amplitude modulation by the beam shaping device, in this case an SLM. Similar to most currently available SLMs, the LC-R2500 used for MISERB does not allow independent field and amplitude modulation. For that reason, a random pixel mask technique similar to [20] can be applied. The amplitude modulation

$$t_{rnd}(x,y) = \Theta(rnd - t(x,y)) \tag{23}$$

is used where rnd is a random number in the interval (0,1) and $t_{LP}(x,y)$ is the amplitude pattern normalized to 1. In this case the amplitude is modulated by the number of pixels that apply a phase shift to the beam. An example is shown in Figs. 8(e), 8(f). The technique will be less efficient if only small parts of the SLM are used, or, it leads to a strong background of undiffracted light if $t(x,y) < 1$ over large areas. In this case an SLM-based alternative would be to use another SLM for amplitude shaping [21]. However, losses are to be expected from the non-unity reflection of the SLM, the polarization rotation coupled to the phase manipulation, and the highly increased free-space propagation distance of the large-diameter beam. An alternative method consists of the grouping of pixels to allow complex field modulation [22,23] at the cost of a reduced effective resolution of the SLM.

5. Illumination beams in homogeneous space

We measured the DOFs of both a Gaussian beam and Bessel beam in homogenuous space. Therefore, a small 45° mirror in the object plane was moved along the optical z-axis to direct illumination light to the detection beam path (see Fig. 1). This enables the direct imaging of the illumination beam's transverse intensity profiles for different z-positions as illustrated in Fig. 9. The coherent imaging process is independent from the PSF of the detection objective (DO), as long as $NA_{DO} > NA_{IO}$. It can be clearly seen in Fig. 9(b) that the Bessel-beam shows thin peaks with a very thin FWHM-width of 0.6µm over a propagation distance of dz≈130µm. Distinct rings are visible surrounding the Bessel beam's peak and even though their amplitude is very small, they carry a considerable amount of energy. In contrast, a conventional beam with a considerably shorter depth of field of roughly 40µm [Fig. 9(a)] has a larger waist size of 1.4µm.

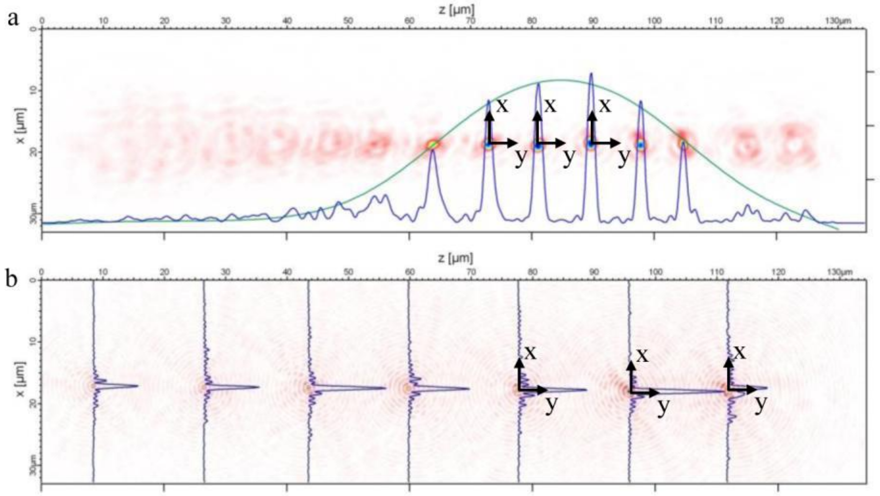

Fig. 9. Direct measurement of the lateral intensity profiles. The graph shows the sum of intensity xy-cross-sections at equally spaced z-positions for a Gaussian beam (a) and a Bessel-beam (b) propagating in homogenous space.

6. Self-reconstruction in inhomogeneous space

For the assessment of the beam's propagation through scattering media, various distributions of silica spheres are used. These are embedded in an Agarose gel cylinder which was fluorescence stained for the visualization of the scattered laser intensity [15]. In contrast to biological material, the beads of known refractive index and size allow a better control over the degree of the inhomogeneity of the medium by which the illumination light is scattered. In many of these cases, the refractive index distribution is easily extractable from the images and thus allows a comparison with results from theory and numerical simulations.

6.1 Two beads in fluorescing gel

A good example for the effect of illumination light scattering by cells is represented by two silica spheres (d = 8µm, n = 1.41), which, in the measurement shown in fig. 10, are positioned along the illumination optical axis at a distance of 70µm. Three illumination beams with equal depth of field are used. A static light sheet formed by a cylindrical lens (a), a laterally scanned Gaussian beam (NA≈0.06), and a laterally scanned Bessel beam (NA≈0.18, ε≈0.88). Figure 10(d) shows an axial intensity profile at the lateral position of the two spheres. The

#134155 - $15.00 USD
Received 7 Sep 2010; accepted 13 Oct 2010; published 4 Nov 2010

profile has a width of b = 16µm and is normalized to the average intensity over a width of b = 60µm for each z-position. The deviation is strongest for the illumination by a light-sheet. In fact, the second sphere is hardly visible due to the strong artifacts. While scattering of a Gaussian illumination beam primarily leads to a very localized increase in intensity by the focusing of the sphere, the profile shown in fig. 10d reveals a significant drop in intensity behind the focii. Artifacts are weakest for illumination by a Bessel beam and the line profile shows that the beam regains its initial intensity shortly behind each of the two scatterers. The experiment is similar to that shown in [15], but the axial distance between the spheres is larger and the beam is scanned over the objects during one single acquisition instead of recording an image at discrete positions of the beam.

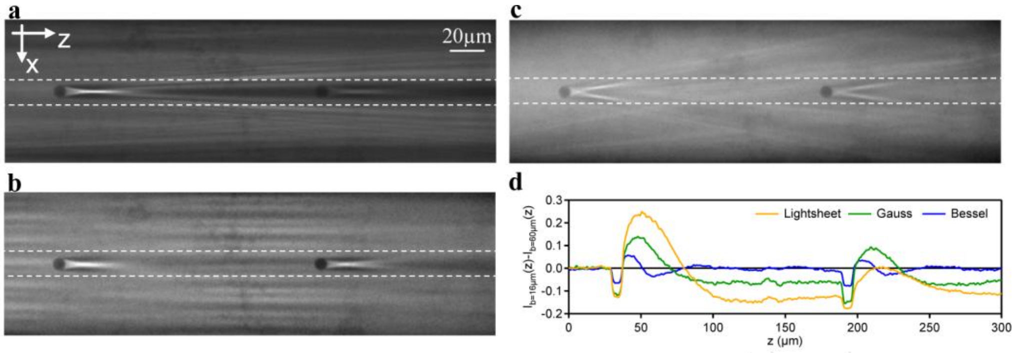

Fig. 10. Images of two silica spheres (d = 8µm). a,b,c, Illumination by a static light sheet (a), a Gaussian beam (b) and a Bessel-beam (c), scanned in x-direction. The difference between z-linescans with widths of b = 16µm (indicated with dashed lines in (a,b,c)) and b = 60µm, $I_{b\,=\,16\mu m}(z)$-$I_{b\,=\,60\mu m}(z)$, is shown in (d).

6.2 A cluster of beads in a fluorescing gel

As an example for a strongly scattering medium a cluster of silica spheres (d = 2µm) fixed in a fluorescing gel cylinder was imaged. The pseudo-color images in Fig. 11 illustrate that relative to the Gaussian beam illumination a Bessel beam illumination leads to much fewer artifacts. Two regions are especially noteworthy. Positions A are good examples for an artifact created by constructive interference of scattered light, whereas at positions B destructive interference leads to shadowing of the illumination beam by a localized aggregate of spheres. Remarkably both effects are strongly reduced by Bessel beam illumination. The normalized lateral standard deviation is a measure for the light-sheet's inhomogeneity [15]. It is given by

$$\hat{s}(z)=\frac{s(z)}{\bar{I}(z)}=\frac{1}{\bar{I}(z)}\sqrt{\frac{1}{dx}\int\left(\bar{I}(z)-I(x,z)\right)^{2}dx} \qquad (24)$$

where $\bar{I}(z)=1/\Delta x\cdot\int_{-\Delta x/2}^{\Delta x/2}I(x,z)dx$ is the lateral intensity average over the image width Δx.

Behind the scatterers $\hat{s}(z)$ is about 2 times larger for the Gaussian beam [see Fig. 11(c)]. Figure 11(d) also shows a lateral intensity linescan $I(x,z$ = 10µm). The deviations for illumination by a Gaussian beam are much more pronounced. Focusing of the illumination light by a sphere leads to a redistribution of the light leading to a positive intensity deviation in the focus created by the sphere and negative deviations on both sides of the focus. For the Bessel beam, this focusing effect is much less distinct. The plane wave wavevectors of the Bessel beam are lying on the surface of a cone with angle α = arcsin(NA/n). Since light is mainly scattered in forward direction, scattered light is distributed over a large solid angle, but only a small part of this cone lies in the focal plane of the detection objective lens. Only this part is imaged sharply and visible as the V-shaped structure behind the sphere.

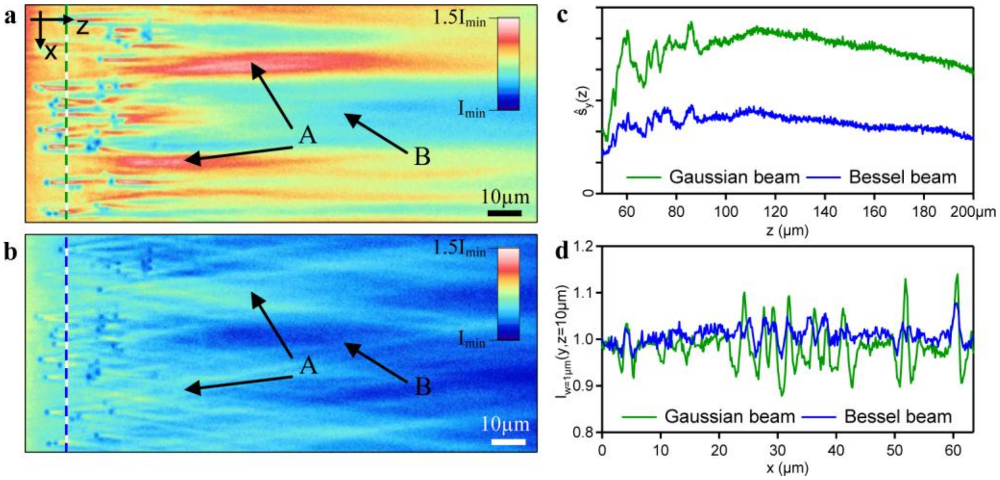

Fig. 11. Imaging of a cluster of silica spheres. a,b, Pseudo-color images of a cluster of silica spheres (d = 2µm) illuminated by a scanned gaussian beam (a), a scanned Bessel beam (b). c, The normalized lateral standard deviation of the image intensity $\hat{s}_x(z)$ as a function of propagation distance z. d, normalized lateral intensity profiles $I(x,z = 10\mu m)$ [position is indicated by the dashed line in (a) and (b)].

6.3 Beam penetration depths for bead clusters

We investigated the penetration of coherent illumination beams into a scattering medium: a fluorescent agarose gel cylinder with a non-uniform density distribution of silica spheres (d = 2µm). For both scanned and static Gaussian and Bessel beam images of two xz-planes for a displacement of the agarose gel cylinder of $\Delta y = 10\mu m$ along the detection optical axis were recorded. In a plane that was entirely free of scatterers, an image of the beam, $I_{hom}(x,z)$ was recorded. Another xz-plane from a region with a high concentration of spheres was selected thus leading to a fluorescence image $I_{inh}(x,z)$ of the scattered beam. The images are shown in Fig. 12(a)–12(d). Both beams feature an equivalent depth of focus, as can be seen from axial intensity linescans with a width of w = 10µm shown in Fig. 12(e).

The intensity distribution of the Gaussian beam shown Fig. 12(c) clearly shows the spreading due to scattering. The beam's focus is almost entirely destroyed in a distance of $z \approx 100\mu m$. The Bessel beam is much less affected by scattering and a pronounced maximum (in green) along the propagation optical axis is maintained even in a depth of 200µm inside the scattering medium [see Fig. 12(d)]. The intensity profile of the beam in the inhomogeneous medium relative to that of the unperturbed beam I_{inh}/I_{hom} is shown in Fig. 12(f). It can be seen, that the intensity of the Gaussian beam drops to 25% of its initial intensity from z = 150µm on. In contrast, the intensity drops to only 60% for the Bessel beam. It is noteworthy, that in the first 50µm the Gaussian and Bessel beam show very similar behavior. The normalized profile of the Bessel beam shows an increase over the last tens of microns. This is partly due to the decreasing $I_{hom}(x,z)$, by which the profile is normalized, but also indicates a strong self-reconstruction ability even deep inside scattering media. The slopes of the curves are independent from the lateral width of the intensity profile.

6.4 Imaging drosophila embryos

As an example for a biological specimen, we imaged a Sytox stained drosophila embryo. Results are shown in Fig. 13. The embryo is illuminated from the left. A stack of 34 images spaced by 2µm along the detection optical y-axis was taken. The stack's maximum projection along the y-axis is shown in Fig. 13(a) for illumination by a Gaussian beam and in Fig. 13(c) for a Bessel beam. Magifications of the regions marked in Fig. 13(a) and 13(c) are shown in fig. b and d. To reach this region, the illumination beam has to propagate a considerable distance through the strongly scattering embryo. It is apparent from the linescans shown in

#134155 - $15.00 USD Received 7 Sep 2010; accepted 13 Oct 2010; published 4 Nov 2010

Fig. 13(e) that the decay of image intensity due to propagation through the sample is clearly less pronounced for illumination by a Bessel beam. This is a consequence of the lower deformation and spreading of the Bessel beam by scattering However, it is also apparent that the Bessel beam does not offer as high contrast as the Gaussian beam. Especially at the front of the object, where the deteriorating effect of the sample on the beam is still weak the image obtained by Gaussian beam illumination reveals higher contrast. For samples with a high density of fluorophores over a large volume, as in this case, a lot of background fluoroscence is excited. The relation between decreased image contrast and improved penetration is as expected. Potential gain in image quality is condition to the possiblity of deminishing the bluring effect of the Bessel beam's ring system on the detection side. The solution to this problem will be adressed in a further study (manuscript in preparation).

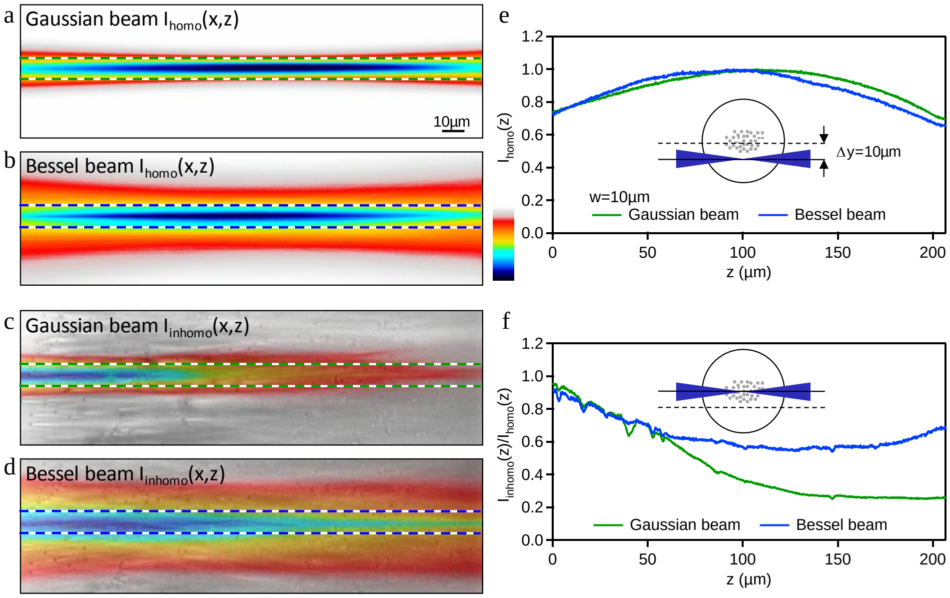

Fig. 12. Measuring the penetration depth of illumination beams in a cluster of silica spheres. a, b, Images of the fluorescence intensity $I_{hom}(x, z)$ in a homogeneous medium for a single static Gaussian beam (a) and Bessel beam (b). c, d, Images of the fluorescence intensity $I_{inh}(x, z)$ of beam's propagation through a cluster of spheres. The pseudo-color image of the intensity of the single beam is overlayed with the grayscale image resulting from a scanned beam. e, Comparison of normalized axial intensity linescans $I_{hom}(0, z)$ with width w = 10µm. d, Comparison of normalized axial intensity linescans for propagation through an inhomogeneous medium $I_{inh}(0, z)$.

7. Summary and conclusion

We presented imaging results and technical details of an add-on module for a light-sheet based microscope using self-reconstructing illumination beams (MISERB). For the illumination of samples we used phase- and amplitude-shaped beams in a direction perpendicular to the detection optical path of a standard inverted microscope. We discussed details of the generation of three different illumination beams using a spatial light modulator: a light sheet, a Gaussian beam, and a Bessel beam. Methods for the manipulation of the hologram for adjustment of the position and depth of field of the different beams were presented.

Due to the orthogonal geometry, in light-sheet based microscopy scattering and absorption effects become more visible than in conventional microscopes. In the latter case the origin of scattering is much harder to detect since they share a common optical axis. The MISERB system described in this study enables a direct comparison of images from exactly the same object, but from different illumination beams. Therefore our setup also represents a useful tool to improve the understanding of light propagation through thick media and the mechanisms of light scattering. This knowledge should be used to further enhance current imaging techniques by minimized light-matter interaction via a control of the beam's phases and amplitude.

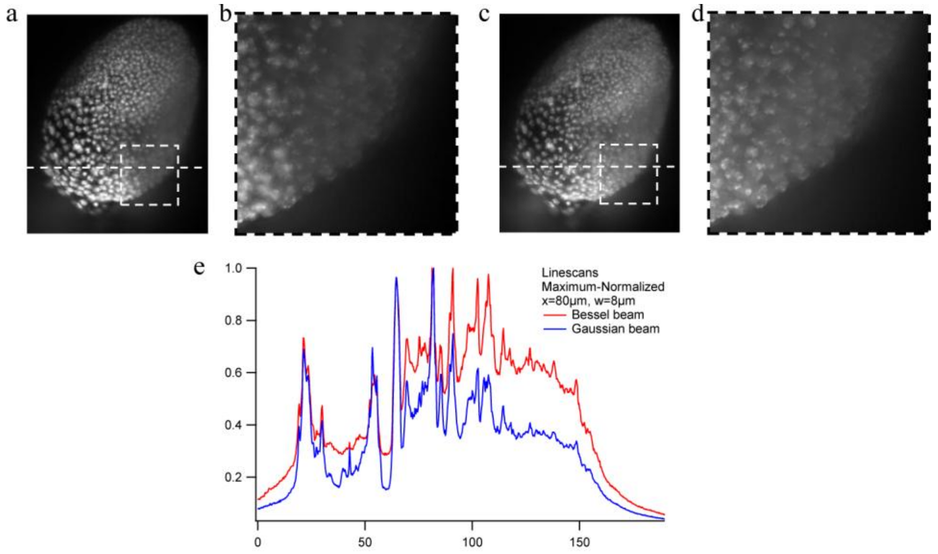

Fig. 13. Images of a drosophila embryo. a-d, The maximum projection of a stack of images for illumination by a Gaussian (a, b) and Bessel beam (c, d). An area of 180µm x230µm is shown in (a) and (c) and the region marked with a size of 75µm x 75µm is shown in (b) and (d). e, An intensity profile in beam propagation direction is shown in e and indicated in (a) and (c) by a dashed line.

Measurements of the propagation of conventional Gaussian beams and Bessel beams in artificial scattering media and a biological sample are shown. By direct comparison to conventional beams we underline that Bessel beams are beneficial for imaging of strongly scattering media. The results indicate that the Bessel-beam's self-reconstruction ability is maintained also in inhomogeneous media. Artifacts resulting from the redistribution of light due to scattering, so called uncorrelated ghost-images, are strongly suppressed. Moreover, an increased penetration depth for strongly scattering media was measured - an effect that offers great potential for the imaging of extended biological specimen such as embryos or tissue.

On the other hand a Bessel-beam carries more energy in its ring system and thereby produces more background intensity. The image contrast is therefore reduced. Ongoing research aims at the reduction of the contrast deteriorating effect of the Bessel beam's ring system. A number of promising approaches are underway.

Acknowledgments

This study was supported by the Excellence Initiative of the German Federal and State Governments (EXC 294). We thank Carl Zeiss MicroImaging GmbH (Jena, Germany) for support in instrument development, B. Wendik for Drosophilae samples, P. v. Olshausen, B. T. Bosworth and C. Gohn-Kreuz for carefully reading the manuscript and valuable comments.